

# Tracking Nanoparticle Degradation across Fuel Cell Electrodes by Automated Analytical Electron Microscopy

Haoran Yu, Michael J. Zachman, Kimberly S. Reeves, Jae Hyung Park, Nancy N. Kariuki, Leiming Hu, Rangachary Mukundan, Kenneth C. Neyerlin, Deborah J. Myers, and David A. Cullen\*



Cite This: *ACS Nano* 2022, 16, 12083–12094



Read Online

ACCESS |

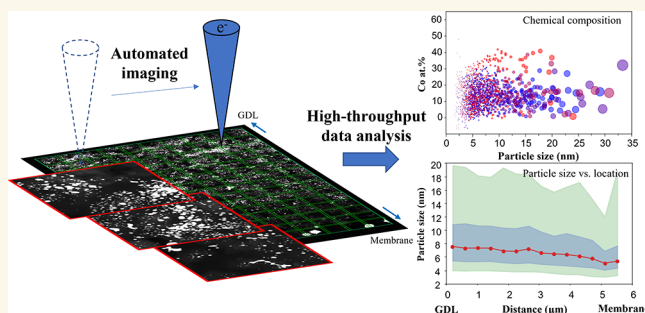
Metrics & More

Article Recommendations

Supporting Information

**ABSTRACT:** Nanoparticles are an important class of materials that exhibit special properties arising from their high surface area-to-volume ratio. Scanning transmission electron microscopy (STEM) has played an important role in nanoparticle characterization, owing to its high spatial resolution, which allows direct visualization of composition and morphology with atomic precision. This typically comes at the cost of sample size, potentially limiting the accuracy and relevance of STEM results, as well as the ability to meaningfully track changes in properties that vary spatially. In this work, automated STEM data acquisition and analysis techniques are employed that enable physical and compositional properties of nanoparticles to be obtained at high resolution over length scales on the order of microns. This is demonstrated by studying the localized effects of potential cycling on electrocatalyst degradation across proton exchange membrane fuel cell cathodes. In contrast to conventional, manual STEM measurements, which produce particle size distributions representing hundreds of particles, these high-throughput automated methods capture tens of thousands of particles and enable nanoparticle size, number density, and composition to be measured as a function of position within the cathode. Comparing the properties of pristine and degraded fuel cells provides statistically robust evidence for the inhomogeneous nature of catalyst degradation across electrodes. These results demonstrate how high-throughput automated STEM techniques can be utilized to investigate local phenomena occurring in nanoparticle systems employed in practical devices.

**KEYWORDS:** automation, nanoparticles, scanning transmission electron microscopy, Python, proton exchange membrane fuel cell



Nanoparticles are studied and used across multiple disciplines, including heterogeneous catalysis,<sup>1–4</sup> energy storage and conversion,<sup>5–8</sup> electronics,<sup>9–11</sup> sensors,<sup>12–14</sup> medicine,<sup>15–18</sup> biomedical engineering,<sup>19–21</sup> and environmental remediation.<sup>22,23</sup> Nanoparticles offer special surface,<sup>24</sup> electronic,<sup>12</sup> optical,<sup>18</sup> magnetic,<sup>25</sup> and catalytic<sup>26</sup> properties due to their high surface area-to-volume ratio and tunable physicochemical characteristics, resulting in enhanced performance compared to their bulk counterparts. For both physical<sup>26–28</sup> and biological systems,<sup>29,30</sup> the performance of nanoparticles can be impacted by both particle size distribution and chemical composition. Current methods for quantifying nanoparticle size distributions include X-ray diffraction (XRD),<sup>31</sup> small-angle X-ray scattering (SAXS),<sup>32</sup> scanning probe microscopy (SPM),<sup>33</sup> and scanning/transmission electron microscopy (S/TEM).<sup>34</sup> STEM is often chosen for nanoparticle characterization when atomic-scale information or local variations in properties are sought, as direct imaging and

spectroscopy can be performed with sub-Ångström spatial resolution.<sup>35,36</sup> However, application of STEM to practical nanoparticle systems used in devices is often met with challenges of statistical significance arising from limitations in the area/quantity of material that can be examined.

For example, STEM is frequently utilized for characterizing proton exchange membrane fuel cell (PEMFC) catalysts,<sup>28,37–40</sup> which typically comprise Pt-based nanoparticles supported on carbon black. Minimizing degradation of the Pt-based oxygen reduction reaction (ORR) cathode catalyst is

Received: March 7, 2022

Accepted: June 23, 2022

Published: July 22, 2022



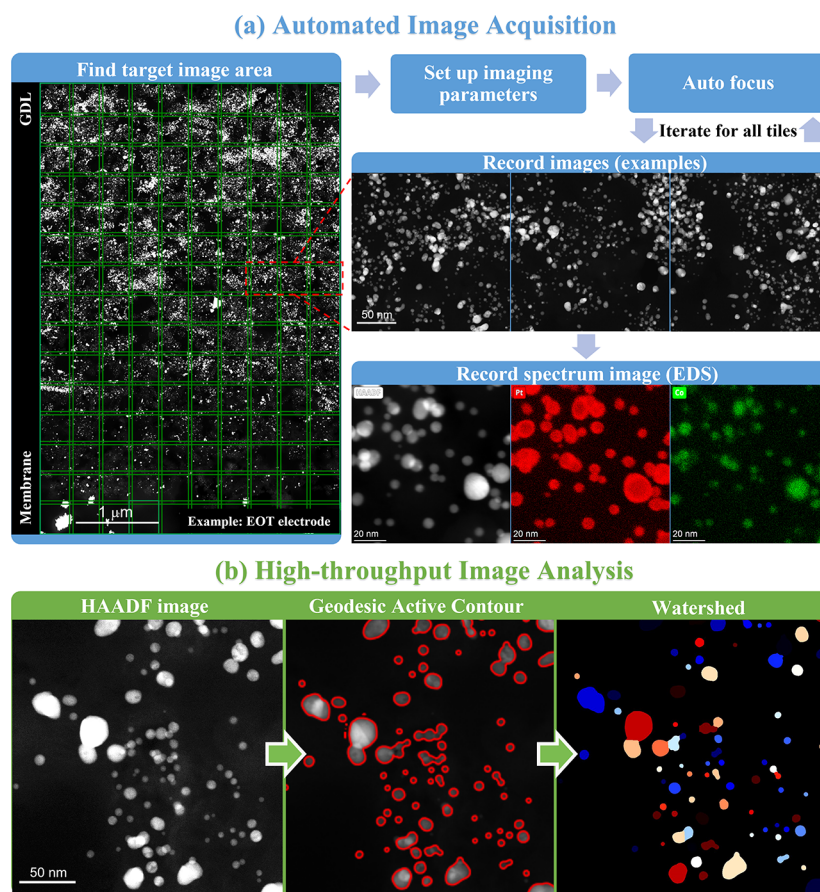


**Figure 1.** Diagram of workflow for (a) automated HAADF-STEM and spectrum image acquisition using the Thermo Scientific MAPS software and (b) high-throughput image analysis using custom python codes employing geodesic active contour and watershed algorithms to measure individual particle properties.

one of the main challenges for implementing PEMFCs in heavy-duty vehicles,<sup>41</sup> where catalyst durability and efficiency become increasingly important.<sup>42</sup> Analysis of the distributions of catalyst particle sizes and compositions is crucial for understanding catalyst degradation during fuel cell operation,<sup>43,44</sup> and STEM can provide direct insight into the relative contributions of different degradation mechanisms, such as Ostwald ripening, particle coalescence/migration, and particle detachment,<sup>37,45</sup> to performance loss. The small volume analyzed during manual instrument operation and time-consuming conventional data analysis methods yield potential operator bias and often poor statistics, with particle size distribution measurements typically limited to hundreds of particles.<sup>28,37–40</sup>

In this work, we employ automated data acquisition and analysis methods that significantly improve the throughput and statistical robustness of STEM particle analysis while reducing operator bias and generating spatially resolved results. Using the PEMFC cathode as a model system, we utilize these techniques to study the local effects of accelerated stress tests (ASTs) on catalyst particle degradation within the cathode. Automated STEM image and energy-dispersive X-ray spectroscopy (EDS) map acquisition using commercial software was paired with high-throughput data analysis using custom Python codes to provide particle size distribution, number density, chemical composition, and precious metal loading as a function of position in the electrode. Using these methods, the physical properties of over 100,000 particles at the beginning

of test (BOT) and 40,000 particles at the end of test (EOT), after 90,000 potential cycles, were analyzed in cross-sectional electrode slices taken from PEMFC membrane electrode assemblies (MEAs). To verify the accuracy of the average automated STEM results, cathode catalyst particle size distributions were determined for the same set of samples using small-angle X-ray scattering (SAXS), a bulk technique providing particle size distributions based on scattering from trillions to quadrillions of particles at typical PEMFC catalyst loadings. In addition, site-specific compositional information was obtained by EDS for thousands of particles for the BOT and EOT electrodes, respectively. Combined, these advancements greatly improve the statistical relevance of STEM data sets, enhance the efficiency in instrument use, reduce human bias and error, and allow spatially resolved information to be obtained across functional devices.

## RESULTS AND DISCUSSION

**Workflow of Automated Imaging and High-Throughput Image Analysis.** The general workflow of automated imaging and high-throughput image analysis is shown in Figure 1. Automated image acquisition was performed using the Thermo Scientific MAPS software. As shown in Figure 1a, the process begins by manually positioning an array of “tiles” over a region of the electrode cross section. A slight overlap allows for minor backlash and drift in the stage movement from one tile to the next to be corrected in postprocessing, in this case using image cross-correlation realized by a custom Python

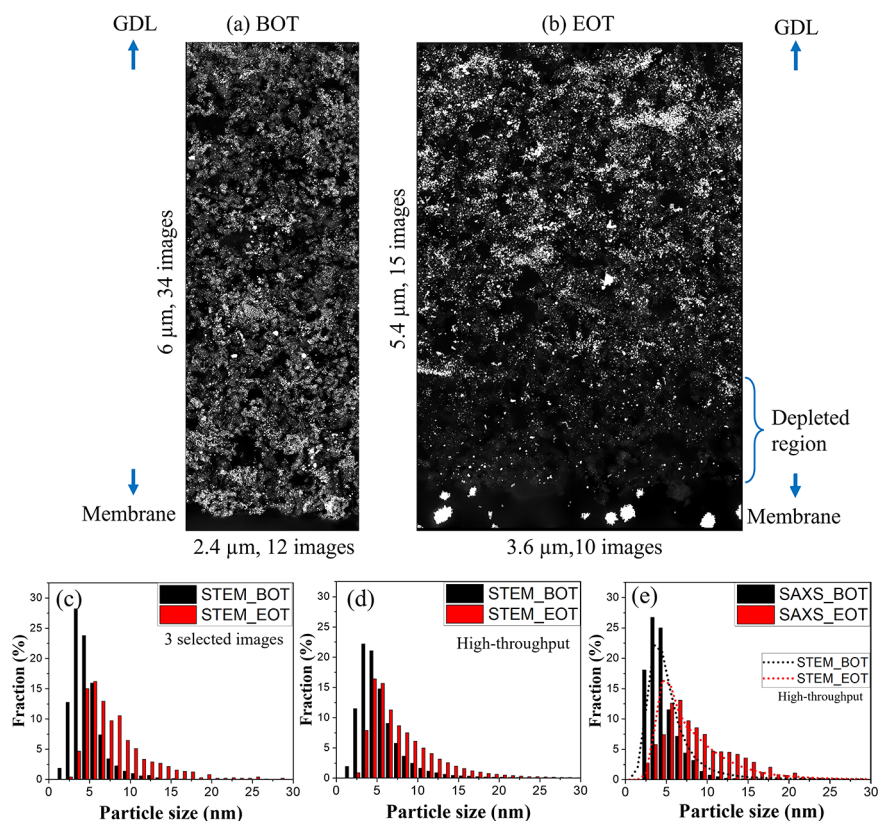


**Figure 2.** Area of MEA cathodes used for particle measurements at (a) BOT and (b) EOT. (c) Particle size distribution obtained from three manually selected images containing a total of  $\sim 1000$  particles for each sample. (d) Particle size distribution obtained from high-throughput STEM analysis of  $\sim 108\text{k}$  particles at BOT and  $\sim 43\text{k}$  particles at EOT. (e) Particle size distribution obtained from SAXS with high-throughput STEM data overlaid in dotted lines.

code. Once the image acquisition parameters are set, the software iteratively moves through the tile set, autofocusing at each position before recording and saving an image. In addition to the high-angle annular dark-field (HAADF) signal, spectroscopic data can also be recorded automatically to correlate particle size with composition. The STEM-EDS arrays cover a smaller area of the electrode due to the longer acquisition times required to generate spectra with sufficient signal-to-noise for reliable quantification.

Following completion of the automated acquisition, the large data sets are transferred to high-performance computers for analysis. Particle size measurements are generally performed by separation of the particle area from the background through thresholding, with additional segmentation to separate overlapping particles. A brief review of this topic can be found in the [Supporting Information](#). Semi-automated procedures following these basic steps have previously been developed to identify and analyze nanoparticles from TEM micrographs.<sup>46–48</sup> Here, we expand on this initial work by fully automating the process<sup>49–60</sup> to provide spatially resolved statistical measurements of physical and compositional properties. [Figure 1b](#) illustrates our workflow for automated particle size measurements from HAADF images. Briefly, the boundaries, or contours, of particles were identified using a morphological geodesic active contour (GAC) method (scikit-image Python package) based on the concept and algorithm introduced previously in the literature.<sup>61–63</sup> The morphological GAC method is able to distinguish particles on a varying background created by the porous carbon support and accurately estimate their

boundaries, whereas more common methods like Otsu thresholding tend to underestimate the particle sizes at this step. To separate overlapping particles, further segmentation was performed using a watershed algorithm (OpenCV Python package). Particle size was then defined as the diameter of a circle with area equal to the particle region. Objects  $< 1$  nm in diameter were excluded from the analysis, as features of this size exclusively originated from morphological GAC artifacts. Particles  $> 30$  nm, which account for  $< 1\%$  of total number of particles, were also excluded as these tended to be dense agglomerates consisting of smaller particles that could not be segmented properly using the watershed algorithm. The coordinates of each particle within a given image were also determined. Combined with positions of the tiles obtained from the automated image acquisition ([Figure 1a](#)), the position of each particle could be determined, allowing spatially resolved measurements to be made. For spectrum images, the segmented particles defined in the simultaneously recorded HAADF-STEM images were used as masks to obtain a summed spectrum for each particle that could be quantified. For additional details on the automated acquisition and analysis, see the [Methods](#) section.

**Particle Size Distribution at BOT vs EOT.** Automated STEM data sets acquired from the cathodes of BOT and EOT MEAs are presented in [Figure 2a,b](#). Each data set is composed of an array of over 100 images spanning the full electrode from the gas diffusion layer (GDL) to the membrane. As average particle size generally increases with cycling, a larger pixel size, and hence reduced number of images, was used to capture the EOT data.



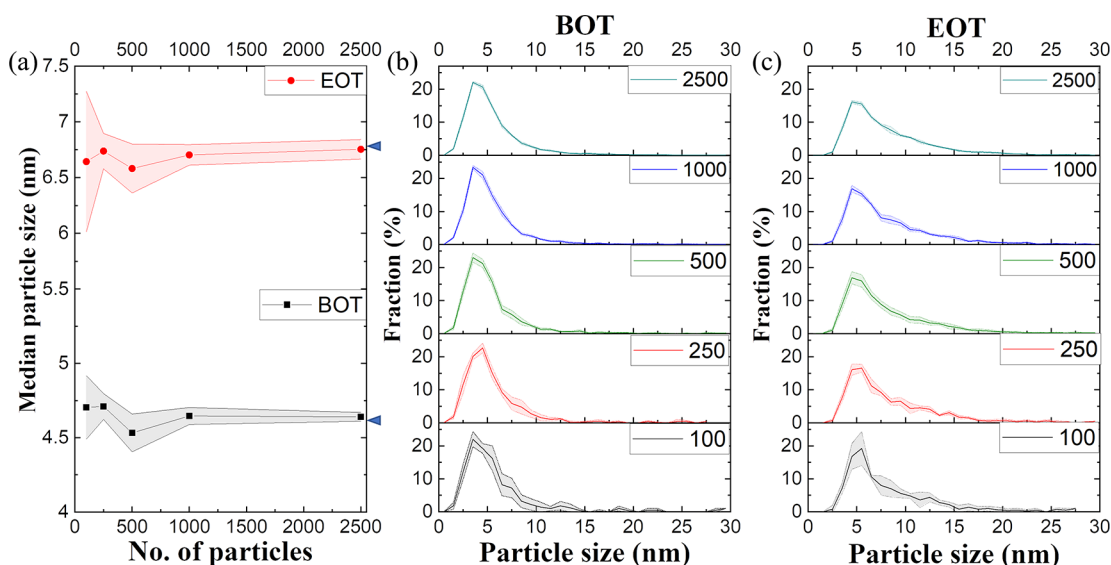


**Figure 3.** (a) Variations in measured median particle size as a function of the number of particles measured. Median particle sizes were measured from five random sets of particles at each sample size, and results are displayed as the mean (points) and standard deviation (shaded regions) of these measurements. Blue arrows indicate median particle sizes from the full data set. (b) BOT and (c) EOT particle size distributions displayed as the means (solid lines) and standard deviations (shaded regions) for the data shown in (a).

Figure 2c shows the particle size distributions obtained from a set of three STEM images containing  $\sim 1000$  particles chosen manually from the image array to avoid agglomerates, as is the typical practice for conventional STEM particle size measurements. This is compared with the particle size distributions of the full BOT and EOT data sets consisting of tens of thousands of particles spanning the full electrode (Figure 2d), along with the particle size distributions of the same MEAs obtained by SAXS (Figure 2e). The overall particle size distributions appear to roughly agree among the three methods, but the conventional approach (Figure 2c) shows more variation in the histogram than the high-throughput analysis (Figure 2d). The particle size distribution obtained using SAXS (Figure 2e) agrees with the STEM data, where the BOT effective particle diameter peaks around 3–4 nm and the EOT peaks above 5 nm with a tail that extends to  $\sim 25$  nm.

To establish the lower limit for the number of particles that must be analyzed to achieve accurate results, we analyzed the effect of sampling on the BOT and EOT particle size distributions. As opposed to Figure 2c, where images avoiding particle agglomerates were intentionally chosen, a random number generator was used to select subsets of particles from the full data set. In this case, no operator bias should be present. Figure 3 shows the results for subsets of the data consisting of 100, 250, 500, 1000, and 2500 randomly selected particles. For each sample size, the random selection process was repeated five times to capture the degree of variation. With increasing sample size, the median particle size gradually trends toward the value of the full data set (indicated by the blue arrows in Figure 3a), and the standard deviation of the measured medians decreases. Correspondingly, the standard deviation in the particle size distributions also decreases with increased sample size. It is noted that the EOT electrode shows higher standard deviation than the BOT electrode because the particle sizes are generally larger and distributed over a wider range as the catalyst degrades. Based on the standard deviations presented Figure 3, at least 1000 particles are recommended for reliable particle size measurement of a given

region. This is consistent with Figure 2c, where the conventional-sized data set, albeit noisier, reasonably matches the larger sample sizes of the automated data set and SAXS measurement. It is acknowledged that this work only examines the through-plane inhomogeneity of catalyst particles from a very small volume of the original MEA. Degraded fuel cell electrodes can also exhibit in-plane particle growth and metal dissolution inhomogeneities depending on the location relative to the gas flow field.<sup>64,65</sup> Capturing these broader variations will be the subject of future efforts.

**Particle Size Variations as a Function of Electrode Position.** In addition to improved statistics, the high-throughput automated STEM approach unlocks the ability to track changes in particle properties as a function of the position across the electrode. For spatially resolved particle size distribution analyses, we separated the overall data sets into sections along the through-plane direction from the GDL to membrane. Each section contained approximately 3000 particles, resulting in section widths of 200 and 400 nm for BOT and EOT, respectively.

Figure 4 shows plots of the variation in particle size between the GDL and membrane for the BOT and EOT cathodes. The red dots represent the median particle size in each slice, the blue region represents the middle 50% of particle sizes, and the green region represents the middle 90% of particle sizes. These results show that the distribution of particle sizes is skewed toward large particles for both the BOT and EOT MEAs. The entire particle size population shifts toward larger sizes after cycling, including the median particle size as well as all boundaries. Along the through-plane direction, the median particle size at BOT is relatively constant, whereas at EOT, the median size decreases from the GDL to the membrane. This phenomenon is attributed to a faster Pt dissolution rate near the membrane, where dissolved Pt ions diffuse quickly toward hydrogen that has crossed over from the anode and are reduced to Pt metal in the membrane.<sup>28,37,66–69</sup> While this has been observed by conventional imaging<sup>28,37,66,67</sup> and derived by modeling<sup>68,69</sup> previously, Figure 4 offers a direct and

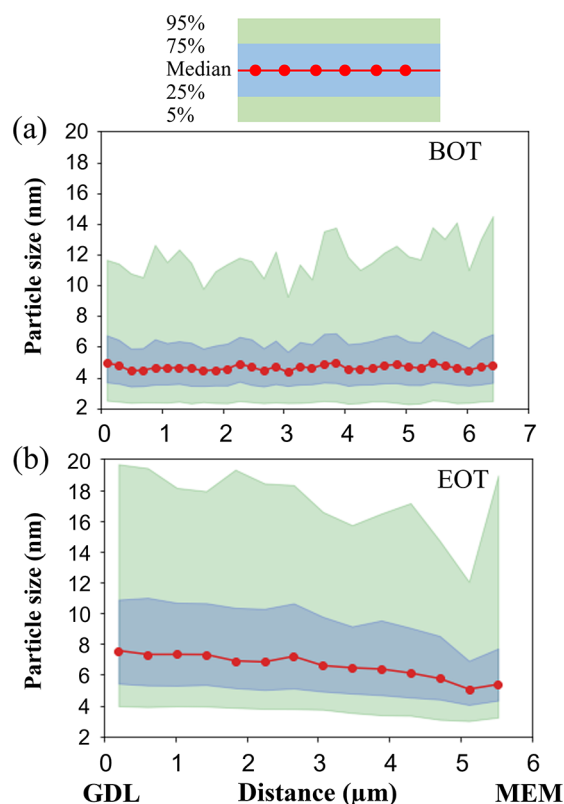


**Figure 4.** Variations in particle size as a function of through-plane position for (a) BOT and (b) EOT electrodes. Median particle sizes (red dots) are plotted along with the middle 50% (blue) and 95% (green) of particle sizes.

statistically robust observation of this trend. In addition, Figure S1 shows particle size distributions corresponding to each point in Figure 4. Interestingly, the fraction of small particles increases near the membrane/cathode interface for the EOT MEA, in agreement with Figure 4b, whereas the distributions at BOT are similar throughout the electrode.

Acquiring images across the whole electrode also enables the absolute number of particles and consequently the catalyst loading to be estimated. This analysis reveals a staggering loss of over 75% of the smaller Pt particles (<10 nm) as a result of AST cycling (Figure 5a–c), which is not fully captured by the change in particle size distribution alone. Figure 5a,b displays the number of particles per square micron across the MEA cross section, termed particle number density, at BOT and EOT, respectively. Figure 5c then displays the estimate of the total particle loading per unit electrode area ( $\text{cm}^2$ ) based on particle number densities in Figure 5a,b and a nominal microtome cross section thickness of 75 nm. Unlike the smaller particles, the number of larger particles and agglomerates (>10 nm) remains mostly unchanged after cycling (Figure S2a), except in the region near the membrane (Figure S2b). According to the Gibbs–Thomson relation, the rate of Pt dissolution increases as Pt particle size decreases.<sup>70</sup> Thus, the more drastic loss of smaller particles relative to larger particles and agglomerates is to be expected. The decreased particle number density near the membrane at EOT suggests enhanced Pt dissolution in this region<sup>28,37,67–69</sup> (Figures 5b and S2b). This is caused by hydrogen crossover from the anode which reduces the dissolved Pt ions into metallic Pt particles near the cathode and further drives the diffusion of Pt ions from the

cathode into the membrane.<sup>68,69</sup> Thus, a depleted region is observed in the region of the cathode near the membrane, and a Pt band is formed in the membrane, as shown in Figure 2b and the STEM-EDS maps of Figure S3. A net Pt loss of ~36% was estimated by taking the ratio of the net Pt-L counts from the electrode to that from the Pt band (Table S1).<sup>50</sup> The significant loss in total precious metal loading was corroborated from the automated particle size measurements by calculating the Pt loading from the particle size distributions. As shown in Figure 5d,e and Figure S2c,d, the Pt loading profile from GDL to the membrane follows a trend similar to that of the number density. The estimation of the total Pt loading at BOT (Figure 5f) is comparable to the nominal Pt loading of  $0.25 \text{ mg}/\text{cm}^2$  as measured by X-ray fluorescence (XRF). In line with the STEM-EDS quantification (Table S1), the estimated Pt loading at EOT dropped by ~25% (Figure 5f), with nearly three-fifths of that loss arising from the dissolution of particles <10 nm in size. It is worth noting in Figure 5f that particles >10 nm contribute to the majority of estimated Pt loading at both BOT and EOT. This agrees with SAXS results where a similar trend can be seen in Table S2. While SAXS measures several orders of magnitude more particles than the high-throughput automated STEM method, Table S2 shows that both techniques arrive at comparable values of median particles and percentages of Pt volume (or loading) attributed to small (<10 nm) and large (>10 nm) particles. Considering that the two techniques sampled different regions from the same MEAs, such agreement provides a strong validation for the high-throughput method developed in this work. Furthermore, the estimated geometric surface area (GSA) between the two techniques is in close agreement with each other and with the MEA measurement of electrochemical surface area (ECSA) of  $34 \text{ m}^2/\text{g}_{\text{Pt}}$  at BOT. The ECSA is measured in a fuel cell using cyclic voltammetry where the adsorption of hydrogen on Pt can be quantified and represents the ratio of the electrochemically active Pt surface area to the Pt loading ( $\text{m}^2/\text{g}_{\text{Pt}}$ ). Conventionally, ECSA calculated at EOT is normalized to the Pt loading at BOT, which convolutes surface area losses from particle growth with Pt migration into the membrane (Figures 5 and S2 and S3). Not surprisingly, the EOT GSA determined by STEM and SAXS are significantly larger than the EOT ECSA, as these values are normalized to the EOT Pt loading. Taking the range in Pt loss (25% from Figure 5f and 36% from Table S1) into account, the ECSA at EOT can be corrected to  $21\text{--}24 \text{ m}^2/\text{g}_{\text{Pt}}$ , which is in good agreement with the high-throughput method and SAXS (Table S2). This analysis also indicates that roughly two-thirds of the ECSA loss originates from particle growth, while the other one-third can be attributed to irreversible Pt migration into the membrane. Operating schemes or specially designed electrode structures which prevent Pt migration out of the electrode may help reduce ECSA losses and consequently improve fuel cell durability.

**Particle Compositions.** The change of Co atomic percent (at. %) relative to Pt, i.e.,  $\text{Pt}_{1-x}\text{Co}_x$  from BOT to EOT is another important indicator of electrocatalyst degradation, as the presence of Co in the nanoparticle core contributes to the enhancement of ORR activity by modifying the surface lattice strain and Pt d-band center of the catalyst particles.<sup>24,28</sup> The Co at. % obtained from wide-angle X-ray scattering (WAXS) (Figure S4) is comparable with STEM-EDS quantification of the spectrum from the entire electrode (Table S3). Averaged line scans extracted from the STEM-EDS maps of the entire

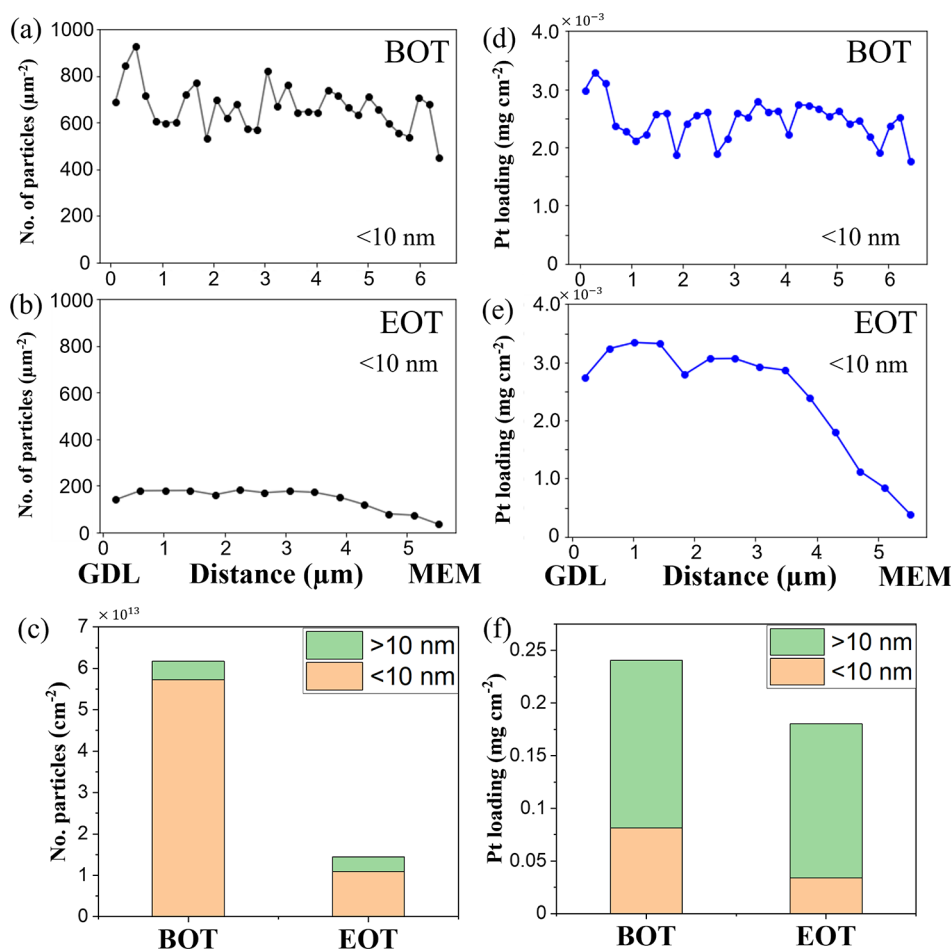


Figure 5. (a,b) Particle number density as a function of through-plane position from the GDL to the membrane at BOT and EOT, respectively. (c) Particle loading at BOT and EOT for particles  $< 10$  nm and  $> 10$  nm. (d,e) Pt loading as a function of through-plane position from the GDL to the membrane at BOT and EOT, respectively. (f) Estimated electrode Pt loading for BOT and EOT.

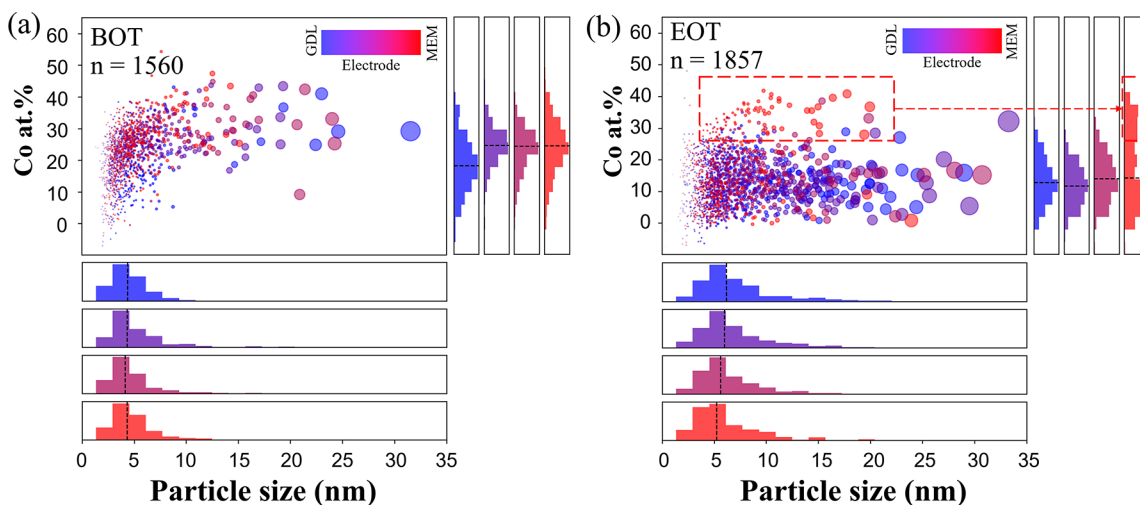
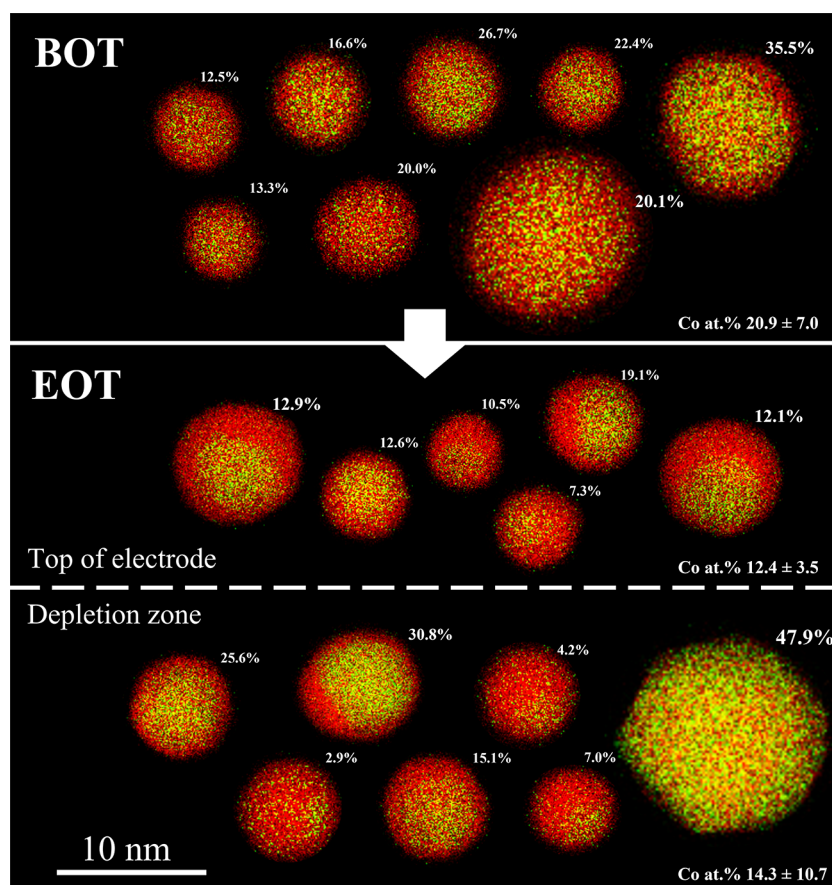


Figure 6. Co atomic percent (at. %) plotted versus particle size (nm) for individual particles as a function of position in the cathode at (a) BOT and (b) EOT. Color indicates the relative position in the cathode. Median values are indicated by the dashed lines in the histograms. BOT and EOT MEA data sets contained 1560 and 1857 particles, respectively. Dashed boxes highlight the particles with high Co content observed near the membrane at EOT.

electrode show an uneven distribution of Co composition for the EOT MEA, as plotted in Figure S5a. Areas near the membrane show relatively higher Co at. % (with higher standard deviation, as well) than the rest of electrode. In

addition to Co leaching, Pt dissolution and redeposition contribute to the relative change of Co at. %. Areas near the membrane show higher loss of PtCo particles and smaller particle size due to a higher Pt dissolution rate (Figures 4 and



**Figure 7.** Overlaid STEM-EDS maps of representative individual nanoparticles showing decrease in (green) Co content and increase in (red) Pt-skin/shell thickness from BOT to EOT. The Co atomic percent (at. %) of each particle is labeled at its top right. The bimodal distribution of low and high Co content nanoparticles in the depletion zone is also shown.

5), which results in a higher net Co at. %. On the other hand, areas near the GDL maintained the BOT Pt loading, despite a large decrease in the total number of particles. This suggests Pt dissolved in these regions is much more likely to redeposit on other particles than move through the electrode and into the membrane. Known as the Ostwald ripening mechanism, Pt from the more rapidly dissolving small particles redeposits onto the larger particles in this process, leading to a concomitant decrease in particle number and increase in particle size. This Pt redeposition has an additive effect with any Co dissolution that occurs, resulting in lower relative Co at. % in regions further away from the membrane.

The automated method allows us to push beyond electrode-level STEM-EDS mapping and conduct a spatially resolved analysis of Co at. % versus particle size across the MEA. Results of automated STEM-EDS mapping and analysis are presented in Figure 6 as scatter plots of Co at. % as a function of particle size, along with the corresponding particle size and Co at. % distributions. The STEM-EDS spectrum images were collected from four areas across the electrode, as indicated in Figure S6. The four regions are color-coded in Figure 6; blue data points represent particles near the GDL, whereas red points represent particles near the membrane. The size of the points is proportional to the particle volumes, based on their measured size and assuming a spherical shape. At BOT, the scatter plots show a wide range of Co at. % for particles <5 nm, from 0 to 40%. As particle size increases, the average Co at. % trends to a higher value until plateauing for particles >10 nm.

Volume averaging all of the particles used in the individual particle measurements yields a decrease in Co at. % from 25–30% at BOT to 10–15% at EOT, in agreement with WAXS and EDS data from the entire electrode (Table S3), and the correlation between Co at. % and particle size becomes less pronounced at EOT. Interestingly, an unexpected bimodal distribution arises for the particles in the depletion zone near the membrane. Here, the automated imaging and high-throughput analysis reveal an ensemble of larger particles (>10 nm) within this depletion zone that exhibit exceptionally high Co at. %, in the range of 30–40%, as indicated by dashed boxes in the scatter plot. This likely contributes to the increased Co at. % near the membrane that was observed in the STEM-EDS line scans spanning the electrode (Figure S5).

To further explore the bimodal distribution revealed in the depletion zone, aberration-corrected STEM-EDS mapping of single particles was performed. Representative particles are shown in Figure 7 at BOT and EOT, with additional data such as size and Co at. % summarized for these particles in Tables S4 and S5 and corresponding HAADF images in Figures S7 and S8. At BOT, Co is distributed homogeneously throughout the particles, with a thin (1–2 monolayer) Pt skin on the surface. By EOT, a strong core–shell morphology emerges, consistent with previous observations,<sup>28,71–74</sup> with most particles exhibiting either a thick, uneven Pt shell over a small PtCo core or showing nearly complete loss of Co from the particle core. Consistent with the bimodal particle composition observed in Figure 6b, a mix of smaller, Co-



depleted nanoparticles and larger, Co-rich nanoparticles were observed in the depleted zone at the EOT. The average Co at. % and its variations measured from individual particle EDS maps fall in line with the high-throughput analysis (Figure 6). The identification of particles with high Co content in the depleted zone shows the benefit of the automated method which led to targeted analysis for high-resolution STEM-EDS mapping. The mechanism behind this bimodal distribution in the depletion zone merits future investigation.

It is worth noting that particle faceting is not obvious after cycling, although some facets can be observed for large particles (>10 nm). Most particles have round edges or close to a spherical shape after cycling. To show the evolution of particle shape after cycling, we calculated eccentricity during the high-throughput analysis. Eccentricity is defined as the ratio of the distance between two focal points and the length of the major axis for an ellipse that has the same normalized second central moments as the region of the particle. An eccentricity of 0 represents a perfect circle. The resulting histograms (Figure S9) show a decreasing trend in eccentricity for particles <10 nm from BOT to EOT, suggesting that particles become more spherical due to degradation. For particles >10 nm, there is no obvious change of the distribution, suggesting that they may be more stable against degradation. The peak at 0.8–0.9 for particles <10 nm could be an artifact due to overlapping particles that are not separated by the software, leading to a highly elliptical shape.

## CONCLUSION

This work demonstrates the combination of high-throughput automated data acquisition and analysis techniques that significantly improve the statistical relevance of STEM-derived nanoparticle size distributions and compositional measurements. The larger data sets allow for changes in particle size distribution, number density, composition, and loading to be determined as a function of location in real devices, demonstrated here using fuel cell electrodes before and after ASTs. We observed that Pt dissolution led to a pronounced loss of small particles, resulting in a shift of the particle size distribution toward larger sizes. In addition, we found that loss of Pt was most severe in the region near the membrane, with this depletion region showing a slightly smaller median particle size compared with the rest of the EOT electrode. The geometric surface area losses from automated STEM and SAXS measurements suggest two-thirds of the observed ECSA losses arise from particle growth, with the other third attributed to Pt migration into the membrane. Individual particle compositions extracted from STEM-EDS spectrum images and paired with size measurements using automated methods revealed an unexpected bimodal distribution in the Co at. % of the alloy nanoparticles in the depletion region near the membrane. This motivated additional targeted high-resolution STEM-EDS mapping, which confirmed the presence of the bimodal distribution. Our results show that automated acquisition and high-throughput analysis can reveal details about the inhomogeneity of catalyst degradation in electrodes that are unavailable by other methods. The methods used in this work are applicable to a range of real devices that contain either supported or unsupported nanoparticles. For heavier supports with varying contrast, such as alumina-supported noble metal catalysts for pyrolysis of biomass, oxidation of CO and hydrocarbons, and water–gas shift reactions, the contrast between the support and particles can be enhanced by

adjusting parameters associated with background removal. As the commonly used watershed has limitations dealing with overlapping particles, future work will focus on better algorithms and explore machine learning for segmenting overlapping particles, which would also be beneficial for characterizing unsupported nanoparticles, such as mixed metal oxide nanoparticles for gas sensing and metal or macro-molecule nanoparticle-based therapeutics.

## METHODS

**Materials.** High surface area carbon (HSC)-supported PtCo (PtCo/HSC, ElystPt500690, Umicore) was used as the cathode catalyst in this study. Catalyst-coated membranes (CCMs) were fabricated by Umicore with a nominal cathode loading of 0.25 mg<sub>Pt</sub>/cm<sup>2</sup> and cathode ionomer to carbon ratio (I/C ratio) of 0.83. The anode utilizes Pt/HSC catalyst (ElystPt200390, Umicore) with a loading of 0.05 mg<sub>Pt</sub>/cm<sup>2</sup>. The CCM was sandwiched between two 50 cm<sup>2</sup> Freudenberg H23C8 (Fuel Cell Store) gas diffusion layers (GDLs) to form the membrane electrode assembly (MEA).

**MEA Testing Protocols.** The MEAs were tested using fuel cell hardware with a 14 channel serpentine flow field and 50 cm<sup>2</sup> active area on both the anode and the cathode and installed with a bolts' torque of 40 in-pounds. The assembled cells were installed with a counter-flow configuration. During the break-in procedure, H<sub>2</sub> and air were supplied to the anode and cathode with a stoichiometric ratio of 0.8 and 2.5. The cell temperature was kept at 80 °C and went through a series of voltage cycles between 0.6 and 0.9 V, with each potential hold of 4 min. The voltage recovery (VR) is conducted by holding the cell voltage at 0.1 V with a flow rate of 0.9 slpm H<sub>2</sub> at the anode and 0.5 slpm air at the cathode for 2 h at 40 °C and 150% RH. The VR improves the electrochemical performance of the cell across the entire fuel cell potential range, as has been previously reported.<sup>75</sup> H<sub>2</sub>/O<sub>2</sub> polarization curves were obtained at 80 °C cell temperature, 100% RH, and 150 kPa backpressure. The current density value was recorded at each cell voltage for 4 min and in an anodic direction from 0.75 V to open-circuit voltage (OCV). H<sub>2</sub>/air polarization curves were obtained at a range of cell temperatures and RH conditions using constant current mode (2.25–0.01 A/cm<sup>2</sup>). The stoichiometric ratios at the anode and cathode are 1.5 and 2, respectively.

The catalyst durability AST was performed by applying square-waveform potential cycling between 0.6 and 0.95 V to the cell. The holding time at each potential was 2.5 s, with a ramping time of 0.5 s and a ramping rate of 700 mV/s between the potential hold. During the AST cycles, the cell was operating at 80 °C in H<sub>2</sub> (anode)/N<sub>2</sub> (cathode) environment and 100% RH. More details can be found in Table P.1 of ref 76. A total of 90,000 (90k) AST cycles were performed.

**Microscopy Sample Preparation and Characterization.** To prepare cross sections of the BOT and EOT cathodes for STEM analysis, portions of the MEA were embedded in epoxy resin and then cut by diamond-knife ultramicrotomy, with a target thickness of ~75 nm. High-angle annular dark-field scanning transmission electron microscopy (HAADF-STEM) and energy-dispersive X-ray spectrum (EDS) images were recorded using a Talos F200X transmission electron microscope (TEM) (Thermo Fisher Scientific) operated at 200 kV and equipped with Super-X EDS system with 4 SDD windowless detectors. The Co composition for each MEA cathode was obtained from EDS elemental maps (21 nm pixel resolution, 10.9 μm field of view) which was processed with the Esprit 1.9 software (Bruker). HAADF images and EDS maps of individual PtCo particles were recorded using a JEM-ARM200F "NEOARM" analytical electron microscope (JEOL Ltd.) operated at 80 kV and equipped with dual SDD windowless detectors each with a 100 nm<sup>2</sup> active area.

**Automated Imaging.** Automated imaging and EDS acquisition were performed on the Talos F200X using the Thermo Scientific MAPS software. Imaging for particle measurements utilized a pixel size of 0.098 nm and a 200 nm field of view for each image of the BOT MEA. Considering the reduced density and increased size of



particles at the EOT, a pixel size of 0.195 and 400 nm field of view were used for the EOT MEA to increase the total imaging area. The 200 kV electron beam was set to a current of  $\sim 600$  pA and a semiconvergence angle of 10.5 mrad. An array of images (tiles) covering the entire cathode cross section was generated using the MAPS software with the above parameters, forming a tile set. Adjacent tiles were overlapped by 10% for alignment during analysis. Automatic focusing was performed for each tile. Automated imaging of the BOT MEA was performed over  $\sim 7$  h for a total of 408 images, acquired overnight without operator intervention or oversight. For the EOT MEA, 150 images were acquired over approximately 2 h of automated imaging time.

Automated STEM-EDS acquisition followed a similar workflow with the addition of recording of a spectrum image before iterating to the next tile. The spectrum image was recorded with the same field of view and semiconvergence angle as the image for particle measurement but with a higher beam current of 2 nA to increase X-ray counts of individual particles. Each spectrum image was recorded with a pixel size of 0.098 nm and a dwell time of 5  $\mu$ s, with a total of 150 drift-corrected frames. Figure S6 shows EDS acquisition areas for each MEA. As each spectrum image requires  $\sim 15$  min acquisition time, the number of EDS maps acquired was fewer than the number of images used for the full electrode particle measurements. Maps were recorded from four zones representing different locations across the cathode. Notably, the zone near the membrane/cathode interface represents the “depleted zone” for the degraded cathode at the EOT. Eight maps were acquired in each zone.

**High-Throughput Automated Image Analysis.** A custom Python code was developed to automatically identify particles in an image and analyze their properties. The code utilized open-source packages including NumPy, SciPy, scikit-image, OpenCV, and Matplotlib and was run on high-performance computing resources in the Compute and Data Environment for Science (CADES) facility at ORNL.

Contour evolution algorithms (morphological GAC)<sup>61</sup> were used to define the boundary of particles. Following the identification of particles, segmentation is performed on overlapping or agglomerated particles using the watershed algorithm which is employed in most works of automated image analysis.<sup>47,52–54,59</sup> Euclidian distance transformation is performed to compute the Euclidean distance to the closest zero of each foreground pixels. The local maxima of the Euclidean distance map are then fed into the watershed function where a matrix of labels is returned. A label value is assigned to each pixel and pixels that have the same label value belong to the same object (particle). Correspondingly, coordinates of the local maxima are regarded as the position of the particle. The relative shifts between neighboring images were then determined by cross-correlation of their overlapping regions, and the particle positions within individual images were combined with these shifts to define the overall positions of the particles within the full image array.

Quantification of spectrum images was performed using a custom Python code on the raw data files recorded by the MAPS software (Thermo Fisher Scientific). Particles with a signal-to-noise ratio threshold below five were not considered for quantification.<sup>77</sup> In this context, “signal” refers to background-subtracted and summed Co-K and Pt-L peak counts, and “noise” is represented by the square root of the total counts at these peaks, including background. The Python codes developed for particle size and compositional analysis are available upon request.

**SAXS/WAXS.** X-ray scattering at beamline 9-ID-C at the Advanced Photon Source was utilized to determine the catalyst particle size and lattice spacings of the PtCo nanoparticles. The cathode catalyst layers were removed from the catalyst-coated membranes using a press and peel technique to transfer the layers to Scotch Magic tape (3M). Monochromatic X-rays with an energy of 21 keV were used and focused to a beam spot size of  $0.8 \times 0.2$  mm. The scattered X-ray intensity was obtained over a range of scattering angles/scatterer dimensions utilizing a Bonse-Hart camera for small-angle X-ray scattering, a Pilatus 100 K detector for pinhole SAXS (pinSAXS) and Dectris detector, which is a modified Pilatus 300 K-W detector, for

wide-angle X-ray scattering.<sup>78,79</sup> The complete scattered intensity,  $I(q)$ , was then obtained by combining the SAXS ( $10^{-4}$  to  $6 \times 10^{-2}$   $\text{\AA}^{-1}$ ) and the pinhole SAXS ( $3 \times 10^{-2}$  to  $1$   $\text{\AA}^{-1}$ ). The WAXS data covered a  $d$ -spacing range from approximately 6 to 0.8  $\text{\AA}$ . Scattering from the Scotch tape was subtracted from that of the cathode catalyst layers. The WAXS data analysis utilized powder diffraction multi peak fitting 2.0, an Irena macro.<sup>80</sup> The position of the (311) scattering peak was utilized to determine the lattice spacing and this spacing was then utilized to calculate the Pt to Co ratio in the crystalline portions of the catalyst particles using Vegard’s law and the nearest neighbor (NN) distances of 2.7747 and 2.4917  $\text{\AA}$  for Pt and Co, respectively. The SAXS data were corrected and reduced with the NIKA software package,<sup>80</sup> and data analysis was conducted using the IRENA software package.<sup>81</sup> Both packages were run on IGOR Pro 7.0 (Wavemetrics). Particle size distributions were obtained from the measured scattering data using the maximum entropy (MaxEnt) method, which involves a constrained optimization of parameters to solve the scattering equation:

$$I(q) = |\Delta Q|^2 \int |F(q, r)|^2 (V(r)) 2N_p(r) dr_{\text{int}} \quad (1)$$

where  $I(q)$  is the scattered intensity,  $q$  is the scattering length density of the particle, and  $F(q, r)$  is the scattering function at scattering vector  $q$  of a particle of characteristic dimension  $r$ .  $V$  is the volume of the particle, and  $N_p$  is the number density of particles in the scattering volume.

## ASSOCIATED CONTENT

### Supporting Information

The Supporting Information is available free of charge at <https://pubs.acs.org/doi/10.1021/acsnano.2c02307>.

Particle size distributions at different locations of the electrode; particle number density and Pt loading for particles  $>10$  nm; analysis of Pt band with EDS mapping; metrics comparing high-throughput and SAXS methods for particle measurements; WAXS data of particle composition; Co distribution from EDS line scans; selected electrode areas for automated particle EDS analysis; EDS analysis of selected individual PtCo particles; evolution of particle shape before and after degradation, and a brief review of nanoparticle measurements from electron microscopy images (PDF)

## AUTHOR INFORMATION

### Corresponding Author

David A. Cullen – Center for Nanophase Materials Sciences, Oak Ridge National Laboratory, Oak Ridge, Tennessee 37831, United States; [orcid.org/0000-0002-2593-7866](https://orcid.org/0000-0002-2593-7866); Email: [cullenda@ornl.gov](mailto:cullenda@ornl.gov)

### Authors

Haoran Yu – Center for Nanophase Materials Sciences, Oak Ridge National Laboratory, Oak Ridge, Tennessee 37831, United States; [orcid.org/0000-0001-7304-2840](https://orcid.org/0000-0001-7304-2840)

Michael J. Zachman – Center for Nanophase Materials Sciences, Oak Ridge National Laboratory, Oak Ridge, Tennessee 37831, United States; [orcid.org/0000-0003-1910-1357](https://orcid.org/0000-0003-1910-1357)

Kimberly S. Reeves – Center for Nanophase Materials Sciences, Oak Ridge National Laboratory, Oak Ridge, Tennessee 37831, United States

Jae Hyung Park – Chemical Sciences and Engineering Division, Argonne National Laboratory, Lemont, Illinois 60439, United States

Nancy N. Kariuki – Chemical Sciences and Engineering Division, Argonne National Laboratory, Lemont, Illinois 60439, United States

Leiming Hu – Chemistry and Nanoscience Center, National Renewable Energy Laboratory, Golden, Colorado 80401, United States

Rangachary Mukundan – Materials Physics and Applications Division, Los Alamos National Laboratory, Los Alamos, New Mexico 87545, United States

Kenneth C. Neyerlin – Chemistry and Nanoscience Center, National Renewable Energy Laboratory, Golden, Colorado 80401, United States; [orcid.org/0000-0002-6753-9698](https://orcid.org/0000-0002-6753-9698)

Deborah J. Myers – Chemical Sciences and Engineering Division, Argonne National Laboratory, Lemont, Illinois 60439, United States; [orcid.org/0000-0001-9299-3916](https://orcid.org/0000-0001-9299-3916)

Complete contact information is available at:

<https://pubs.acs.org/10.1021/acsnano.2c02307>

### Author Contributions

The manuscript was written through contributions from all authors. All authors have given approval to the final version of the manuscript. D.A.C. conceived the idea and implemented automated imaging protocols. H.Y. and M.J.Z. developed the Python code for data analysis. K.S.R. and H.Y. performed automated imaging. L.H., K.C.N., and R.M. developed and performed the MEA ASTs. K.S.R. prepared ultramicrotome slices of BOT and EOT MEAs. J.H.P., N.N.K., and D.J.M. performed SAXS measurements and related data analysis.

### Notes

The authors declare no competing financial interest.

This manuscript has been authored in part by UT-Battelle, LLC, under contract DE-AC05-00OR22725 with the U.S. Department of Energy (DOE). The U.S. government retains and the publisher, by accepting the article for publication, acknowledges that the U.S. government retains a nonexclusive, paid-up, irrevocable, worldwide license to publish or reproduce the published form of this manuscript, or allow others to do so, for U.S. government purposes. DOE will provide public access to these results of federally sponsored research in accordance with the DOE Public Access Plan (<http://energy.gov/downloads/doe-public-access-plan>).

### ACKNOWLEDGMENTS

This material is based on work performed by the Million Mile Fuel Cell Truck (M2FCT) Consortium, technology managers Greg Kleen and Dimitrios Papageorgopoulos, which is supported by the U.S. Department of Energy, Office of Energy Efficiency and Renewable Energy, Hydrogen and Fuel Cell Technologies Office. For more information, visit <https://millionmilefuelcelltruck.org>. Electron microscopy research was supported by the Center for Nanophase Materials Sciences (CNMS), which is a U.S. Department of Energy, Office of Science User Facility at Oak Ridge National Laboratory. The Talos F200X S/TEM tool was provided by U.S. DOE, Office of Nuclear Energy, Fuel Cycle R&D Program, and the Nuclear Science User Facilities. The X-ray scattering experiments were performed at beamline 9-ID-C at the Advanced Photon Source (APS) at Argonne National Laboratory (ANL). Use of the APS, an Office of Science user facility operated by ANL, is supported by the U.S. Department of Energy, Office of Science, Office of Basic Energy Sciences, under Contract No. DE-AS02-06CH11357. This work was authored in part by

Alliance for Sustainable Energy, LLC, the manager and operator of the National Renewable Energy Laboratory for the U.S. Department of Energy under Contract No. DE-AC36-08GO28308, Los Alamos National Laboratory under Contract No. 89233218CNA000001 operated by Triad National Security, LLC, for the National Nuclear Security Administration of U.S. Department of Energy, and UT-Battelle, LLC, under contract DE-AC05-00OR22725 with the U.S. Department of Energy.

### REFERENCES

- (1) Bell, A. T. The Impact of Nanoscience on Heterogeneous Catalysis. *Science* (80-) **2003**, 299 (5613), 1688–1691.
- (2) Cuenya, B. R. Synthesis and Catalytic Properties of Metal Nanoparticles: Size, Shape, Support, Composition, and Oxidation State Effects. *Thin Solid Films* **2010**, 518 (12), 3127–3150.
- (3) Tachikawa, T.; Fujitsuka, M.; Majima, T. Mechanistic Insight into the TiO<sub>2</sub> Photocatalytic Reactions: Design of New Photocatalysts. *J. Phys. Chem. C* **2007**, 111 (14), 5259–5275.
- (4) Liu, L.; Corma, A. Metal Catalysts for Heterogeneous Catalysis: From Single Atoms to Nanoclusters and Nanoparticles. *Chem. Rev.* **2018**, 118 (10), 4981–5079.
- (5) Guo, S.; Wang, E. Noble Metal Nanomaterials: Controllable Synthesis and Application in Fuel Cells and Analytical Sensors. *Nano Today* **2011**, 6 (3), 240–264.
- (6) Su, X.; Wu, Q.; Li, J.; Xiao, X.; Lott, A.; Lu, W.; Sheldon, B. W.; Wu, J. Silicon-Based Nanomaterials for Lithium-Ion Batteries: A Review. *Adv. Energy Mater.* **2014**, 4 (1), 1300882.
- (7) Shao, M.; Chang, Q.; Dodelet, J.-P.; Chenitz, R. Recent Advances in Electrocatalysts for Oxygen Reduction Reaction. *Chem. Rev.* **2016**, 116 (6), 3594–3657.
- (8) Kodama, K.; Nagai, T.; Kuwaki, A.; Jinnouchi, R.; Morimoto, Y. Challenges in Applying Highly Active Pt-Based Nanostructured Catalysts for Oxygen Reduction Reactions to Fuel Cell Vehicles. *Nat. Nanotechnol.* **2021**, 16 (2), 140–147.
- (9) Kamyshny, A.; Magdassi, S. Conductive Nanomaterials for Printed Electronics. *Small* **2014**, 10 (17), 3515–3535.
- (10) Trindade, T.; O'Brien, P.; Pickett, N. L. Nanocrystalline Semiconductors: Synthesis, Properties, and Perspectives. *Chem. Mater.* **2001**, 13 (11), 3843–3858.
- (11) Konstantatos, G.; Sargent, E. H. Nanostructured Materials for Photon Detection. *Nat. Nanotechnol.* **2010**, 5 (6), 391–400.
- (12) Miller, D. R.; Akbar, S. A.; Morris, P. A. Nanoscale Metal Oxide-Based Heterojunctions for Gas Sensing: A Review. *Sensors Actuators B Chem.* **2014**, 204, 250–272.
- (13) Holzinger, M.; Le Goff, A.; Cosnier, S. Nanomaterials for Biosensing Applications: A Review. *Front. Chem.* **2014**, 2, 63.
- (14) Zhu, C.; Yang, G.; Li, H.; Du, D.; Lin, Y. Electrochemical Sensors and Biosensors Based on Nanomaterials and Nanostructures. *Anal. Chem.* **2015**, 87 (1), 230–249.
- (15) Zhang, L.; Gu, F. X.; Chan, J. M.; Wang, A. Z.; Langer, R. S.; Farokhzad, O. C. Nanoparticles in Medicine: Therapeutic Applications and Developments. *Clin. Pharmacol. Ther.* **2008**, 83 (5), 761–769.
- (16) Dreaden, E. C.; Alkilany, A. M.; Huang, X.; Murphy, C. J.; El-Sayed, M. A. The Golden Age: Gold Nanoparticles for Biomedicine. *Chem. Soc. Rev.* **2012**, 41 (7), 2740–2779.
- (17) Kumar, C. S. S. R.; Mohammad, F. Magnetic Nanomaterials for Hyperthermia-Based Therapy and Controlled Drug Delivery. *Adv. Drug Delivery Rev.* **2011**, 63 (9), 789–808.
- (18) Cheng, L.; Wang, C.; Feng, L.; Yang, K.; Liu, Z. Functional Nanomaterials for Phototherapies of Cancer. *Chem. Rev.* **2014**, 114 (21), 10869–10939.
- (19) Chaloupka, K.; Malam, Y.; Seifalian, A. M. Nanosilver as a New Generation of Nanoproduct in Biomedical Applications. *Trends Biotechnol.* **2010**, 28 (11), 580–588.

- (20) Erathodiyl, N.; Ying, J. Y. Functionalization of Inorganic Nanoparticles for Bioimaging Applications. *Acc. Chem. Res.* **2011**, *44* (10), 925–935.
- (21) Wang, F.; Banerjee, D.; Liu, Y.; Chen, X.; Liu, X. Upconversion Nanoparticles in Biological Labeling, Imaging, and Therapy. *Analyst* **2010**, *135* (8), 1839–1854.
- (22) Khin, M. M.; Nair, A. S.; Babu, V. J.; Murugan, R.; Ramakrishna, S. A Review on Nanomaterials for Environmental Remediation. *Energy Environ. Sci.* **2012**, *5* (8), 8075–8109.
- (23) Hua, M.; Zhang, S.; Pan, B.; Zhang, W.; Lv, L.; Zhang, Q. Heavy Metal Removal from Water/Wastewater by Nanosized Metal Oxides: A Review. *J. Hazard. Mater.* **2012**, *211–212*, 317–331.
- (24) Stamenkovic, V.; Mun, B. S.; Mayrhofer, K. J. J.; Ross, P. N.; Markovic, N. M.; Rossmeisl, J.; Greeley, J.; Nørskov, J. K. Changing the Activity of Electrocatalysts for Oxygen Reduction by Tuning the Surface Electronic Structure. *Angew. Chemie Int. Ed.* **2006**, *45* (18), 2897–2901.
- (25) Lu, A.-H.; Salabas, E. L.; Schüth, F. Magnetic Nanoparticles: Synthesis, Protection, Functionalization, and Application. *Angew. Chemie Int. Ed.* **2007**, *46* (8), 1222–1244.
- (26) Shao, M.; Peles, A.; Shoemaker, K. Electrocatalysis on Platinum Nanoparticles: Particle Size Effect on Oxygen Reduction Reaction Activity. *Nano Lett.* **2011**, *11* (9), 3714–3719.
- (27) Stamenkovic, V. R.; Mun, B. S.; Arenz, M.; Mayrhofer, K. J. J.; Lucas, C. A.; Wang, G.; Ross, P. N.; Markovic, N. M. Trends in Electrocatalysis on Extended and Nanoscale Pt-Bimetallic Alloy Surfaces. *Nat. Mater.* **2007**, *6* (3), 241–247.
- (28) Chen, S.; Sheng, W.; Yabuuchi, N.; Ferreira, P. J.; Allard, L. F.; Shao-Horn, Y. Origin of Oxygen Reduction Reaction Activity on “Pt3Co” Nanoparticles: Atomically Resolved Chemical Compositions and Structures. *J. Phys. Chem. C* **2009**, *113* (3), 1109–1125.
- (29) Albanese, A.; Tang, P. S.; Chan, W. C. W. The Effect of Nanoparticle Size, Shape, and Surface Chemistry on Biological Systems. *Annu. Rev. Biomed. Eng.* **2012**, *14* (1), 1–16.
- (30) Shang, L.; Nienhaus, K.; Nienhaus, G. U. Engineered Nanoparticles Interacting with Cells: Size Matters. *J. Nanobiotechnology* **2014**, *12* (1), 5.
- (31) Leng, Y. X-Ray Diffraction Methods. *Materials Characterization*; Wiley-VCH Verlag GmbH & Co. KGaA: Weinheim, Germany, 2013; Vol. 25, pp 47–82.
- (32) Leng, Y. X-Ray Spectroscopy for Elemental Analysis. *Materials Characterization*; Wiley-VCH Verlag GmbH & Co. KGaA: Weinheim, Germany, 2013; Vol. 25, pp 191–219.
- (33) Leng, Y. Scanning Probe Microscopy. *Materials Characterization*; Wiley-VCH Verlag GmbH & Co. KGaA: Weinheim, Germany, 2013; Vol. 25, pp 163–189.
- (34) Leng, Y. Transmission Electron Microscopy. *Materials Characterization*; Wiley-VCH Verlag GmbH & Co. KGaA: Weinheim, Germany, 2013; Vol. 25, pp 83–126.
- (35) Chung, H. T.; Cullen, D. A.; Higgins, D.; Sneed, B. T.; Holby, E. F.; More, K. L.; Zelenay, P. Direct Atomic-Level Insight into the Active Sites of a High-Performance PGM-Free ORR Catalyst. *Science* (80-.). **2017**, *357* (6350), 479–484.
- (36) Li, J.; Sharma, S.; Liu, X.; Pan, Y.-T.; Spendlow, J. S.; Chi, M.; Jia, Y.; Zhang, P.; Cullen, D. A.; Xi, Z.; Lin, H.; Yin, Z.; Shen, B.; Muzzio, M.; Yu, C.; Kim, Y. S.; Peterson, A. A.; More, K. L.; Zhu, H.; Sun, S. Hard-Magnet L10-CoPt Nanoparticles Advance Fuel Cell Catalysis. *Joule* **2019**, *3* (1), 124–135.
- (37) Ferreira, P. J.; la O', G. J.; Shao-Horn, Y.; Morgan, D.; Makharia, R.; Kocha, S.; Gasteiger, H. A. Instability of Pt/C Electrocatalysts in Proton Exchange Membrane Fuel Cells. *J. Electrochem. Soc.* **2005**, *152* (11), A2256.
- (38) Gummalla, M.; Ball, S. C.; Condit, D. A.; Rasouli, S.; Yu, K.; Ferreira, P. J.; Myers, D. J.; Yang, Z. Effect of Particle Size and Operating Conditions on Pt3Co PEMFC Cathode Catalyst Durability. *Catalysts* **2015**, *5*, 926.
- (39) Rasouli, S.; Ortiz Godoy, R. A.; Yang, Z.; Gummalla, M.; Ball, S. C.; Myers, D.; Ferreira, P. J. Surface Area Loss Mechanisms of Pt3Co Nanocatalysts in Proton Exchange Membrane Fuel Cells. *J. Power Sources* **2017**, *343*, S71–S79.
- (40) Ramaswamy, N.; Kumaraguru, S.; Gu, W.; Kukreja, R. S.; Yu, K.; Groom, D.; Ferreira, P. High-Current Density Durability of Pt/C and PtCo/C Catalysts at Similar Particle Sizes in PEMFCs. *J. Electrochem. Soc.* **2021**, *168* (2), 024519.
- (41) Borup, R. L.; Kusoglu, A.; Neyerlin, K. C.; Mukundan, R.; Ahluwalia, R. K.; Cullen, D. A.; More, K. L.; Weber, A. Z.; Myers, D. J. Recent Developments in Catalyst-Related PEM Fuel Cell Durability. *Curr. Opin. Electrochem.* **2020**, *21*, 192–200.
- (42) Cullen, D. A.; Neyerlin, K. C.; Ahluwalia, R. K.; Mukundan, R.; More, K. L.; Borup, R. L.; Weber, A. Z.; Myers, D. J.; Kusoglu, A. New Roads and Challenges for Fuel Cells in Heavy-Duty Transportation. *Nat. Energy* **2021**, *6* (5), 462–474.
- (43) Papadias, D. D.; Ahluwalia, R. K.; Kariuki, N.; Myers, D.; More, K. L.; Cullen, D. A.; Sneed, B. T.; Neyerlin, K. C.; Mukundan, R.; Borup, R. L. Durability of Pt-Co Alloy Polymer Electrolyte Fuel Cell Cathode Catalysts under Accelerated Stress Tests. *J. Electrochem. Soc.* **2018**, *165* (6), F3166–F3177.
- (44) O'Brien, T. E.; Herrera, S.; Langlois, D. A.; Kariuki, N. N.; Yu, H.; Zachman, M. J.; Myers, D. J.; Cullen, D. A.; Borup, R. L.; Mukundan, R. Impact of Carbon Support Structure on the Durability of PtCo Electrocatalysts. *J. Electrochem. Soc.* **2021**, *168* (5), 054517.
- (45) Borup, R.; Meyers, J.; Pivovar, B.; Kim, Y. S.; Mukundan, R.; Garland, N.; Myers, D.; Wilson, M.; Garzon, F.; Wood, D.; Zelenay, P.; More, K.; Stroh, K.; Zawodzinski, T.; Boncella, J.; McGrath, J. E.; Inaba, M.; Miyatake, K.; Hori, M.; Ota, K.; Ogumi, Z.; Miyata, S.; Nishikata, A.; Siroma, Z.; Uchimoto, Y.; Yasuda, K.; Kimijima, K.; Iwashita, N. Scientific Aspects of Polymer Electrolyte Fuel Cell Durability and Degradation. *Chem. Rev.* **2007**, *107* (10), 3904–3951.
- (46) Park, C.; Huang, J. Z.; Huitink, D.; Kundu, S.; Mallick, B. K.; Liang, H.; Ding, Y. A Multistage, Semi-Automated Procedure for Analyzing the Morphology of Nanoparticles. *IEEE Trans.* **2012**, *44* (7), 507–522.
- (47) De Temmerman, P.-J.; Verleysen, E.; Lammertyn, J.; Mast, J. Semi-Automatic Size Measurement of Primary Particles in Aggregated Nanomaterials by Transmission Electron Microscopy. *Powder Technol.* **2014**, *261*, 191–200.
- (48) Reichelt, W. N.; Kaineder, A.; Brillmann, M.; Neutsch, L.; Taschauer, A.; Lohninger, H.; Herwig, C. High Throughput Inclusion Body Sizing: Nano Particle Tracking Analysis. *Biotechnol. J.* **2017**, *12* (6), 1600471.
- (49) Laramy, C. R.; Brown, K. A.; O'Brien, M. N.; Mirkin, C. A. High-Throughput, Algorithmic Determination of Nanoparticle Structure from Electron Microscopy Images. *ACS Nano* **2015**, *9* (12), 12488–12495.
- (50) Padgett, E.; Yarlagadda, V.; Holtz, M. E.; Ko, M.; Levin, B. D. A.; Kukreja, R. S.; Ziegelbauer, J. M.; Andrews, R. N.; Ilavsky, J.; Kongkanand, A.; Muller, D. A. Mitigation of PEM Fuel Cell Catalyst Degradation with Porous Carbon Supports. *J. Electrochem. Soc.* **2019**, *166* (4), F198–F207.
- (51) Zafari, S.; Eerola, T.; Ferreira, P.; Kälviäinen, H.; Bovik, A. In *Automated Segmentation of Nanoparticles in BF TEM Images by U-Net Binarization and Branch and Bound BT - Computer Analysis of Images and Patterns*; Vento, M., Percannella, G., Eds.; Springer International Publishing: Cham, Switzerland, 2019; pp 113–125.
- (52) Slater, T. J. A.; Wang, Y.-C.; Leteba, G. M.; Quiroz, J.; Camargo, P. H. C.; Haigh, S. J.; Allen, C. S. Automated Single-Particle Reconstruction of Heterogeneous Inorganic Nanoparticles. *Microsc. Microanal.* **2020**, *26* (6), 1168–1175.
- (53) Horwath, J. P.; Zakharov, D. N.; Mégret, R.; Stach, E. A. Understanding Important Features of Deep Learning Models for Segmentation of High-Resolution Transmission Electron Microscopy Images. *npj Comput. Mater.* **2020**, *6* (1), 108.
- (54) Kim, H.; Han, J.; Han, T. Y.-J. Machine Vision-Driven Automatic Recognition of Particle Size and Morphology in SEM Images. *Nanoscale* **2020**, *12* (37), 19461–19469.



- (55) Gordon, O. M.; Hodgkinson, J. E. A.; Farley, S. M.; Hunsicker, E. L.; Moriarty, P. J. Automated Searching and Identification of Self-Organized Nanostructures. *Nano Lett.* **2020**, *20* (10), 7688–7693.
- (56) Frei, M.; Kruis, F. E. Image-Based Size Analysis of Agglomerated and Partially Sintered Particles via Convolutional Neural Networks. *Powder Technol.* **2020**, *360*, 324–336.
- (57) Liz, M. F.; Nartova, A. V.; Matveev, A. V.; Okunev, A. G. Using Computer Vision and Deep Learning for Nanoparticle Recognition on Scanning Probe Microscopy Images: Modified U-Net Approach. *2020 Science and Artificial Intelligence conference (S.A.I.lence)* **2020**, 13–16.
- (58) ILETT, M.; WILLS, J.; REES, P.; SHARMA, S.; MICKLETHWAITE, S.; BROWN, A.; BRYDSON, R.; HONDOW, N. Application of Automated Electron Microscopy Imaging and Machine Learning to Characterise and Quantify Nanoparticle Dispersion in Aqueous Media. *J. Microsc.* **2020**, *279* (3), 177–184.
- (59) Rühle, B.; Krumrey, J. F.; Hodoroba, V.-D. Workflow towards Automated Segmentation of Agglomerated, Non-Spherical Particles from Electron Microscopy Images Using Artificial Neural Networks. *Sci. Rep.* **2021**, *11* (1), 4942.
- (60) Uusimäki, T.; Wagner, T.; Lipinski, H.-G.; Kaegi, R. AutoEM: A Software for Automated Acquisition and Analysis of Nanoparticles. *J. Nanoparticle Res.* **2019**, *21* (6), 122.
- (61) Márquez-Neila, P.; Baumela, L.; Alvarez, L. A Morphological Approach to Curvature-Based Evolution of Curves and Surfaces. *IEEE Trans. Pattern Anal. Mach. Intell.* **2014**, *36* (1), 2–17.
- (62) Kass, M.; Witkin, A.; Terzopoulos, D. Snakes: Active Contour Models. *Int. J. Comput. Vis.* **1988**, *1* (4), 321–331.
- (63) Caselles, V.; Kimmel, R.; Sapiro, G. Geodesic Active Contours. *Int. J. Comput. Vis.* **1997**, *22* (1), 61–79.
- (64) Cheng, L.; Khedekar, K.; Rezaei Talarposhti, M.; Perego, A.; Metzger, M.; Kuppen, S.; Stewart, S.; Atanassov, P.; Tamura, N.; Craig, N.; Zenyuk, I. V.; Johnston, C. M. Mapping of Heterogeneous Catalyst Degradation in Polymer Electrolyte Fuel Cells. *Adv. Energy Mater.* **2020**, *10* (28), 2000623.
- (65) Khedekar, K.; Rezaei Talarposhti, M.; Besli, M. M.; Kuppen, S.; Perego, A.; Chen, Y.; Metzger, M.; Stewart, S.; Atanassov, P.; Tamura, N.; Craig, N.; Cheng, L.; Johnston, C. M.; Zenyuk, I. V. Probing Heterogeneous Degradation of Catalyst in PEM Fuel Cells under Realistic Automotive Conditions with Multi-Modal Techniques. *Adv. Energy Mater.* **2021**, *11* (35), 2101794.
- (66) Yu, H.; Baricci, A.; Bisello, A.; Casalegno, A.; Guetaz, L.; Bonville, L.; Maric, R. Strategies to Mitigate Pt Dissolution in Low Pt Loading Proton Exchange Membrane Fuel Cell: I. A Gradient Pt Particle Size Design. *Electrochim. Acta* **2017**, *247*, 1155–1168.
- (67) Yu, H.; Baricci, A.; Casalegno, A.; Guetaz, L.; Bonville, L.; Maric, R. Strategies to Mitigate Pt Dissolution in Low Pt Loading Proton Exchange Membrane Fuel Cell: II. A Gradient Pt Loading Design. *Electrochim. Acta* **2017**, *247*, 1169–1179.
- (68) Jahnke, T.; Futter, G. A.; Baricci, A.; Rabissi, C.; Casalegno, A. Physical Modeling of Catalyst Degradation in Low Temperature Fuel Cells: Platinum Oxidation, Dissolution, Particle Growth and Platinum Band Formation. *J. Electrochem. Soc.* **2020**, *167* (1), 013523.
- (69) Zheng, Z.; Luo, L.; Zhu, F.; Cheng, X.; Yang, F.; Shen, S.; Wei, G.; Zhang, J. Degradation of Core-Shell Pt<sub>3</sub>Co Catalysts in Proton Exchange Membrane Fuel Cells (PEMFCs) Studied by Mathematical Modeling. *Electrochim. Acta* **2019**, *323*, 134751.
- (70) Tang, L.; Han, B.; Persson, K.; Friesen, C.; He, T.; Sieradzki, K.; Ceder, G. Electrochemical Stability of Nanometer-Scale Pt Particles in Acidic Environments. *J. Am. Chem. Soc.* **2010**, *132* (2), 596–600.
- (71) Yu, C.; Koh, S.; Leisch, J. E.; Toney, M. F.; Strasser, P. Size and Composition Distribution Dynamics of Alloy Nanoparticle Electrocatalysts Probed by Anomalous Small Angle X-Ray Scattering (ASAXS). *Faraday Discuss.* **2009**, *140* (0), 283–296.
- (72) Dubau, L.; Maillard, F.; Chatenet, M.; Guetaz, L.; Andre, J.; Rossinot, E. Durability of Pt[Sub 3]Co/C Cathodes in a 16 Cell PEMFC Stack: Macro/Microstructural Changes and Degradation Mechanisms. *J. Electrochem. Soc.* **2010**, *157* (12), B1887.
- (73) Lopez-Haro, M.; Dubau, L.; Guétaz, L.; Bayle-Guillemaud, P.; Chatenet, M.; André, J.; Caqué, N.; Rossinot, E.; Maillard, F. Atomic-Scale Structure and Composition of Pt<sub>3</sub>Co/C Nanocrystallites during Real PEMFC Operation: A STEM–EELS Study. *Appl. Catal. B Environ.* **2014**, *152–153* (1), 300–308.
- (74) Gilbert, J. A.; Kropf, A. J.; Kariuki, N. N.; DeCrane, S.; Wang, X.; Rasouli, S.; Yu, K.; Ferreira, P. J.; Morgan, D.; Myers, D. J. In-Operando Anomalous Small-Angle X-Ray Scattering Investigation of Pt<sub>3</sub>Co Catalyst Degradation in Aqueous and Fuel Cell Environments. *J. Electrochem. Soc.* **2015**, *162* (14), F1487–F1497.
- (75) Kabir, S.; Myers, D. J.; Kariuki, N.; Park, J.; Wang, G.; Baker, A.; Macauley, N.; Mukundan, R.; More, K. L.; Neyerlin, K. C. Elucidating the Dynamic Nature of Fuel Cell Electrodes as a Function of Conditioning: An Ex Situ Material Characterization and in Situ Electrochemical Diagnostic Study. *ACS Appl. Mater. Interfaces* **2019**, *11* (48), 45016–45030.
- (76) Hydrogen and Fuel Cell Technologies Office Multi-Year Research, Development, and Demonstration Plan; [https://www.energy.gov/sites/prod/files/2017/05/f34/fcto\\_myrrdd\\_fuel\\_cells.pdf](https://www.energy.gov/sites/prod/files/2017/05/f34/fcto_myrrdd_fuel_cells.pdf) (accessed 2022-02-08).
- (77) Rose, A. The Sensitivity Performance of the Human Eye on an Absolute Scale\*. *J. Opt. Soc. Am.* **1948**, *38* (2), 196–208.
- (78) Ilavsky, J.; Jemian, P. R.; Allen, A. J.; Zhang, F.; Levine, L. E.; Long, G. G. Ultra-Small-Angle X-Ray Scattering at the Advanced Photon Source. *J. Appl. Crystallogr.* **2009**, *42* (3), 469–479.
- (79) Ilavsky, J.; Zhang, F.; Allen, A. J.; Levine, L. E.; Jemian, P. R.; Long, G. G. Ultra-Small-Angle X-Ray Scattering Instrument at the Advanced Photon Source: History, Recent Development, and Current Status. *Metall. Mater. Trans. A* **2013**, *44* (1), 68–76.
- (80) Ilavsky, J. Nika: Software for Two-Dimensional Data Reduction. *J. Appl. Crystallogr.* **2012**, *45* (2), 324–328.
- (81) Ilavsky, J.; Jemian, P. R. Irena: Tool Suite for Modeling and Analysis of Small-Angle Scattering. *J. Appl. Crystallogr.* **2009**, *42* (2), 347–353.